



## A comparison of AA2024 and AA7150 subjected to ultrasonic shot peening: Microstructure, surface segregation and corrosion



Qingqing Sun<sup>a,b</sup>, Xingtao Liu<sup>a</sup>, Qingyou Han<sup>a,\*</sup>, Jie Li<sup>b</sup>, Rong Xu<sup>c</sup>, Kejie Zhao<sup>c</sup>

<sup>a</sup> School of Engineering Technology, Purdue University, West Lafayette, IN 47907, United States

<sup>b</sup> School of Chemistry and Chemical Engineering, Central South University, Changsha, Hunan 410012, China

<sup>c</sup> School of Mechanical Engineering, Purdue University, West Lafayette, IN 47907, United States

### ARTICLE INFO

#### Keywords:

AA2024

AA7150

Ultrasonic shot peening

Surface nanocrystallization

Surface segregation

Corrosion

### ABSTRACT

The influence of ultrasonic shot peening (USSP) on microstructure, surface segregation, localized and electrochemical corrosion of AA2024 was investigated using immersion test, OCP, EIS, polarization, XRD and SEM-EDS methods. The results are compared with those of AA7150. Like AA7150, second phase particles of AA2024 peened surface layer dissolved into Al matrix due to the extended solid solubility caused by USSP. After USSP, corrosion rate of AA2024 increased by 2–3 times due to surface contamination, however, intergranular corrosion (IGC) resistance of AA2024 is significantly enhanced by USSP treatment. The improvement in localized corrosion resistance is mainly attributed to grain refinement and microstructure homogenization. As opposed to AA7150, OCP of AA2024 in 3.5 wt% NaCl solution (pH = 5.8) shifts to more noble direction after USSP. This is due to the different surface segregation behaviours of the two studied alloys. The mechanism of surface segregation is also briefly discussed.

### 1. Introduction

Surface mechanical attrition treatment (SMAT) is one technique that can induce severe plastic deformation (SPD) on the surface of alloys, resulting in a strain hardening, grain refinement and induction of compressive stress [1–3]. Ultrasonic shot peening (USSP) is a relative novel method of SMAT to achieve surface SPD. There is a significant body of research regarding the corrosion properties of alloys subjected to SMAT/USSP. However, due to the complex nature of corrosion, both beneficial and deleterious effects caused by SMAT have been reported. For instance, beneficial effects of SMAT/SPD on corrosion rate of Al alloys were reported by several researchers [4–6]. However, Mustafa Abdulstaar [7], R.A. Waikar [8] and M. Navaser [9] reported that SMAT deteriorated corrosion resistance of Al alloys. The effect of SMAT on corrosion performance varies with alloy system [10,11], grain orientation [4], corrosive environment [12], temperature [13], impact parameters [14] and etc.

A detailed understanding of corrosion behavior observed for surface nanocrystallization processed materials is, however, lacking [15]. Briefly, two critical aspects in corrosion research of surface nanocrystallization processed materials have long been ignored. The first one is the localized corrosion nature of many alloys. Compared with uniform corrosion, localized corrosion, such as pitting, IGC and SCC, are more

common and more dangerous for Al alloys, especially for 2000 and 7000 series ultra-high strength Al alloys. Therefore, corrosion depth, rather than corrosion rate which can be easily derived from electrochemical curves, deserves more attention from researchers. Unfortunately, most of the published work only studied corrosion rate using electrochemical methods [7–13,16–21]. Only a few authors noticed this and measured corrosion depth in their work [4,5]. Another frequently ignored aspect is the galvanic corrosion interaction. After SPD processing, especially after surface SPD treatment, the electrochemical potential of the new formed layer of alloy changed, due to segregation of elements [22], grain refinement [1,2,23] and redistribution of elements at grain boundaries and in the matrix [24], change of passive oxide film [13] and sometimes, foreign impurities induced [22]. The potential difference between nanocrystalline surface layer and interior will, definitely, result in electron transfer and galvanic corrosion.

Previous work [22,25] has investigated the effects of USSP on electrochemical and localized corrosion of AA7150. In this work, surface nanocrystallization, surface contamination and surface segregation of AA2024 and AA7150 caused by USSP were reported and compared, and their influences on corrosion behaviours of these two aircraft alloys were studied and compared using XRD, SEM, immersion, OCP, EIS and polarization methods.

\* Corresponding author.

E-mail address: [hanq@purdue.edu](mailto:hanq@purdue.edu) (Q. Han).

**Table 1**  
Compositions of AA2024 and AA7150 (wt%).

Alloys	Zn	Mg	Cu	Mn	Si	Fe	Cr	Zr	Others	Al
AA2024	0.13	0.57	4.6	0.57	0.08	0.19	0.01	0.00	0.11	Balance
AA7150	6.5	2.3	2.3	0.1	0.12	0.15	0.04	0.10	0.21	Balance

## 2. Experimental

### 2.1. Materials and USSP setup

AA2024 was a rolled plate, received from Kaiser Aluminum Corp. and treated with temper T351. AA7150 plate was received from Alcoa Corp., rolled and treated with T7751 aging process. The compositions of the two studied alloys are listed in Table 1. The main alloying elements are Al-Mg-Cu for AA2024, while the main alloying elements are Al-Zn-Mg-Cu for AA7150. The USSP setup and parameters are described elsewhere [22].

### 2.2. Intergranular corrosion test

According to ASTM standard, G110-9257 g/L NaCl + 10 mL/L H<sub>2</sub>O<sub>2</sub> was chosen as testing solution for corrosion depth. The exposure was conducted at room temperature for 24 h, in a vessel holding 15 mL of testing solution per square cm of specimen surface area. After exposure, each specimen was rinsed with water and the cross-section of the exposure surface was etched with Keller' reagent. The maximum corrosion depth of more than 15 images (each image was 2.679 mm in length and corresponded to a maximum depth) was measured. Then the average value of maximum corrosion depths and the maximum depth of all the obtained images was calculated and compared for the untreated and USSPed alloys. The untreated represents specimen without USSP treatment but receives the same treatment prior to USSP.

### 2.3. XRD and SEM

XRD patterns were performed using a Bruker D-8 Focus X-ray diffractometer with CuK<sub>α</sub> radiation and at a 2θ scanning rate of 4°/min to determine the phase constituents in the surface layer. β<sub>hkl</sub>, which is full width at half maximum (FWHM), was determined using Jade software (MDI JADE 7 Materials Data XRD Pattern Processing, Identification, and Quantification). The value of β<sub>hkl</sub> can be described by Eq. (1) [26], from which the values of mean microstrain and nanocrystalline grain

size can be derived.

$$\beta_{\text{hkl}}^2 - \beta_0^2 = \left( \frac{K \lambda}{D_{\text{hkl}} \cos \theta} \right)^2 + (4\epsilon \tan \theta)^2 \quad (1)$$

where  $K$  is a numerical factor frequently referred to as the crystallite-shape factor ( $K = 0.89$  for Al),  $\lambda$  is the wavelength of incident wave,  $D_{\text{hkl}}$  is the crystallite size in the direction perpendicular to the lattice planes,  $hkl$  are the Miller indices of the planes being analysed, and  $\theta$  is the Bragg angle,  $\epsilon$  is microstrain,  $\beta_0$  is the instrumental broadening.

The cross-section of the peened specimen, etched by Keller's reagent (containing 95 mL of reagent water, 2.5 mL of nitric acid (70%), 1.5 mL of hydrochloric acid (37%) and 1.0 mL of hydrofluoric acid (48%)), were characterized by Phenom Desktop scanning electron microscopy (SEM) using BSE mode. Energy dispersive X-ray spectroscopy (EDS) line and mapping scan were performed to characterize surface elements segregation and surface contamination phenomena of alloys after USSP treatment.

### 2.4. Electrochemical test

A VersaSTAT 3 potentiostat/galvanostat connected to a three-electrode cell was used for the electrochemical measurements. The working electrode was the test material with an immersed area of 1.0 cm<sup>2</sup>. Platinum gauze and saturated calomel (SCE) electrodes were used as the counter and reference electrodes, respectively. Electrochemical tests were performed in naturally aerated 3.5 wt% NaCl solution. Open circuit potential (OCP) - time curves were measured for alloys subjected to USSP and 1 month natural aging treatments. Electrochemical impedance spectroscopy (EIS) measurements were conducted when OCP was stable, with the frequency ranging from 100 kHz to 0.1 Hz and the amplitude of the sinusoidal potential signal was 10 mV with respect to the OCP. Polarization curves were obtained at a scan rate of 0.2 mV/s, ranging from  $-0.3 V_{\text{OCP}}$  to  $0.3 V_{\text{OCP}}$ . All electrochemical tests were performed under room temperature in a faraday cage. To ensure the reproducibility of the results, experiments were repeated at least three times under the same experimental condition.

## 3. Results

### 3.1. Microstructure

Cross-sectional SEM backscattered electron images of AA2024 without and with USSP treatment are shown in Fig. 1a and b respectively. The original grain size of the rolled plate was 50–100 μm wide. The thickness of the USSP

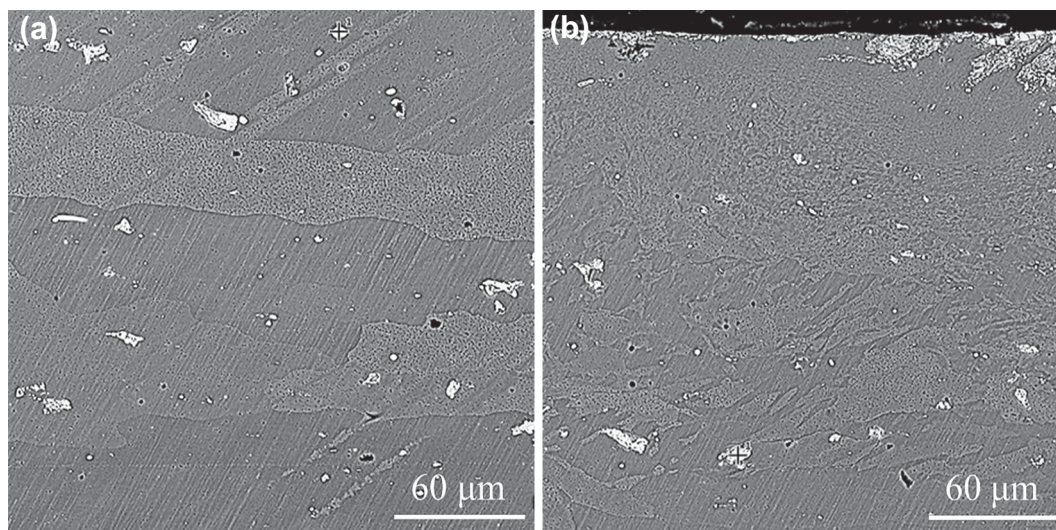


**Fig. 1.** Cross-sectional SEM backscattered electron images of AA2024: (a) as-received; (b) USSP treated.

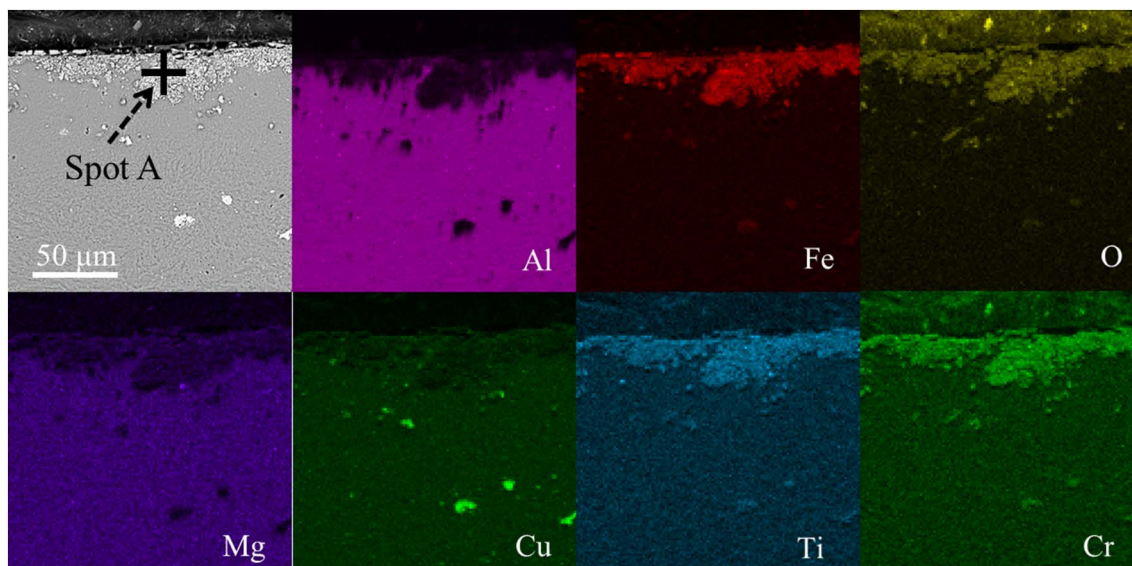


Fig. 2. Surface contaminated layer of USSP treated AA2024 and its corresponding EDS elements mapping.

affected area was about 200  $\mu\text{m}$ . After USSP, severe grain refinement and distortion effects can be easily seen. Actually, it has been extensively reported that alloys with gradient microstructure were achieved through SMAT/USSP, with grain size down to nano-regime in the topmost surface layer [13,15,27–31]. Surface nanocrystallization of AA2024 generated by USSP [32,33] and esonix ultrasonic impact treatment [34] has been reported. Our previous work [25] also demonstrated that nanocrystalline structure formed on AA7150 USSP treated surface layer.

### 3.2. Surface contamination

As seen from Fig. 2, surface contamination layer with thickness 5–30  $\mu\text{m}$  was observed for the AA2024 after USSP treatment. The EDS spectra reveals that the composition (Table 2) of “Spot A” in Fig. 2 mainly contains 29.6 wt% Al, 36.1 wt% Fe, 25.5 wt% O, 4.9 wt% Ti, 0.6 wt% Cr and 0.0 wt% Ni. Therefore, it can be concluded that the contaminated layer was mostly from the cast iron enclosure and Ti-6Al-4 V ultrasonic converter, rather than from S440 stainless steel balls. Our previous work [22] showed similar results were found for AA7150. Surface contaminated layer containing 38.9 wt% Fe and 1.4 wt% Ti, with thickness of about 20  $\mu\text{m}$ , coated on surface layer of the USSP treated AA7150 [22]. Note that the contaminated layer was not evenly distributed on the surface of alloys. In literature, other researchers reported that surface contamination was found on pure Mg [35] and AA2024 [21] after SMAT. The presence of contamination layer increased the corrosion rate of these alloys [21,35] and may cover the beneficial effect of SMAT, which is quite misleading.

### 3.3. Surface segregation

From the EDS line scan profile shown in Fig. 3a, Cu and Fe were found segregating in the topmost 15  $\mu\text{m}$  thick peened surface layer of AA2024. However, as seen from Fig. 3b, Zn and Cu segregated in the topmost surface layer of the peened AA7150 [22]. EDS line scan characterization was performed on the uncontaminated area of the

cross-sectional SEM images of the peened alloys. Before EDS characterization, both USSP treated alloys were naturally aged for 1 month (electrochemical tests were also conducted for alloys subjected to USSP and 1 month natural aging). One thing should be noted that, instead of accurate composition, EDS line scan can only reflect the composition trend as a function of depth. For instance, the mass fraction of Cu in AA2024 substrate as determined by EDS line scan is about 10 wt%, which is higher than the actual value (4.6 wt%). EDS point scan can measure chemical composition with a better accuracy; the point scan data obtained are listed in Table 3. In the very topmost layer ( $\sim 1 \mu\text{m}$  from surface) of the peened AA2024, Cu increased from 4.5 to 8.4 wt%, Fe increased from 0.2 to 1.9 wt%. As a result, the content of Al and Mg on surface layer decreased. Similarly, for AA7150, Zn and Cu in the very topmost peened layer increased from 6.1 wt% and 2.1 wt% to 14.3 wt% and 4.4 wt%, respectively, and consequently mass fraction of Al and Mg declined [22].

Surface segregation was due to the diffusion of elements from sub-surface to surface layer. The driving force of diffusion is solid solubility difference. By introducing large number of vacancies through USSP treatment, it is expected to assume that solid solubility of alloying elements in Al matrix increased after USSP treatment. Solid solubility extension of iron in the aluminum matrix for an Al-11 wt% Fe alloy after processing with high pressure torsion was reported by Senkov et al. [36]. The equilibrium solubility of iron in aluminum lattice is very low and even at high temperature it does not exceed 0.05 wt%. However, during high pressure torsion treatment, the maximum solubility of iron in Al lattice increases to 2.2 wt%. Thus, it is believed that the supersaturated solid solution on the surface layer turns to be unsaturated after USSP treatment. Therefore, thermodynamically, solutes like Zn, Cu, Fe and Mg are expected to diffuse from supersaturated area (sub-surface layer or substrate) to unsaturated area (surface layer). The segregating atoms in surface layer are in the form of solid solution rather than new-formed phases, as will be revealed by XRD results in the next section.

Assuming that surface layer is a precipitate, the needed diffusion efficiencies for Zn and Cu can be roughly estimated using Zener's equation (Eqs. (2)–(3)) [37].

$$S = \alpha_1 \sqrt{Dt} \quad (2)$$

$$\alpha_1 = (n_\infty - n_1) / \sqrt{(n_0 - n_1)(n_0 - n_\infty)} \quad (3)$$

where  $S$  is the diffusion distance,  $\alpha_1$  is the growth coefficient,  $n_\infty$  is the concentration of the element in the matrix far away from the

Table 2

EDS elements composition (wt%) of “Spot A” shown in Fig. 2.

Al	Fe	O	Ti	Cu	Mg	Cr	Ni
29.6	36.1	25.5	4.9	2.1	0.4	0.6	0.0

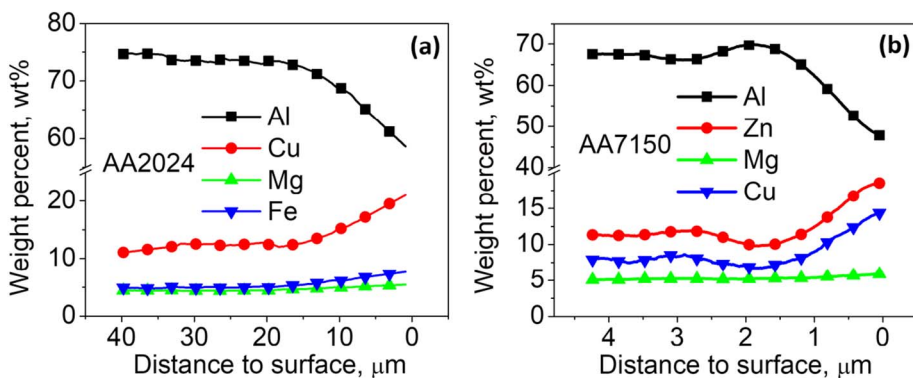


Fig. 3. SEM-EDS line scan profile of USSP treated alloys after 1 month natural aging: (a) AA2024; (b) AA7150 [22].

Table 3

EDS point scan compositions (wt%) of the substrates and surfaces of the two USSP treated alloys.

Alloys	Point	Al	Zn	Mg	Cu	Fe
AA2024	Substrate	92.7	/	2.6	4.5	0.2
	Surface	88	/	1.7	8.4	1.9
AA7150	Substrate	88.2	6.1	3.4	2.1	0.2
	Surface	79.2	14.3	1.8	4.4	0.3

precipitate,  $n_0$  is the concentration of the element in the precipitate,  $n_1$  is the concentration of the element in the matrix that is in equilibrium with the precipitate.

For AA2024, the values of diffusion efficiencies of Cu and Fe are expected to be close to  $D_{Cu} = 1.57 \times 10^{-16} \text{ m}^2/\text{s}$  and  $D_{Fe} = 7.57 \times 10^{-15} \text{ m}^2/\text{s}$ , respectively. For AA7150, the values of diffusion efficiencies of Zn and Cu are expected to be close to  $D_{Zn} = 1.35 \times 10^{-17} \text{ m}^2/\text{s}$  and  $D_{Cu} = 4.80 \times 10^{-18} \text{ m}^2/\text{s}$ , respectively. However, these estimated values are  $\sim 10$  orders of magnitude higher than diffusion efficiencies of these elements in Al lattice under room temperature [38]. Therefore, an alternative diffusion mechanism must be responsible. It is believed that “short circuit” paths, such as grain boundaries or dislocation pipes, are accountable for the fast diffusion behaviour. Under room temperature, diffusion efficiencies of elements along grain boundaries can be 7–16 orders of magnitude higher than the values along lattice [38–41]. For instance,  $D_{Zn}$ ,  $4.64 \times 10^{-21} \text{ m}^2/\text{s}$  along subgrain boundary,  $5.58 \times 10^{-18} \text{ m}^2/\text{s}$  along high-angle GB with high activation energy, and  $5.08 \times 10^{-15} \text{ m}^2/\text{s}$  along high-angle GB with low activation energy [38], are comparable with the estimated value of  $D_{Zn} = 1.35 \times 10^{-17} \text{ m}^2/\text{s}$  obtained using Zener's equation.  $D_{Cu}$  is  $1.74 \times 10^{-19} \text{ m}^2/\text{s}$  as calculated from GB concentration profile in depth and is  $1.18 \times 10^{-18} \text{ m}^2/\text{s}$  as calculated from data of contour angle [41]. Again, literature data of  $D_{Cu}$  along grain boundaries at least is comparable to the estimated values ( $D_{Cu} = 1.57 \times 10^{-16} \text{ m}^2/\text{s}$  for AA2024 and  $4.80 \times 10^{-18} \text{ m}^2/\text{s}$  for AA7150). Differently from Zn and Cu, Mg was depleted on alloys surface layer. This is due to the negative value of Mg-vacancy binding energy [42–44], which results in a much slower diffusion kinetics than Cu and Zn.

### 3.4. XRD

Fig. 4 shows the XRD patterns of AA2024 with and without USSP & 1 month natural aging treatments. Though large amount of iron-rich surface contamination was induced, iron phases were absent from XRD patterns [21,22]. This might be due to small grain size effect (less than 10 nm) of foreign iron particles or due to amorphous state of iron formed during the repetitive attrition process [21,22]. Therefore, XRD patterns shown in Fig. 4 only reflect the phase properties of grain refined layer.

The as-received AA2024 is a rolled plate with highly preferred

orientation (200), as can be seen in Fig. 4a. By comparing the relative intensities of XRD peaks of peened samples with the calculated Al data (ICDD PDF number 85-1327 [45]), it can be roughly concluded that for USSP treated AA2024, the grain orientation in the very topmost surface layer is nearly random. Like AA2024, random orientation was also observed for AA7150 subjected to USSP [22]. Compared the patterns of AA2024 with and without USSP shown in Fig. 4b, several peaks marked with inverted triangle on the patterns of as-received sample disappeared after the USSP and natural aging treatments, demonstrating the dissolving of second phase particles. For AA2024, the dissolved phases mainly are  $\theta$  phase ( $\text{Al}_2\text{Cu}$ ) and S phase ( $\text{Al}_2\text{CuMg}$ ) [46–48]. For AA7150 [22,25] the dissolved phase mainly is  $\eta'$  and  $\eta$  phase ( $\text{MgZn}_2$ ) [49–51]. Murayama et al. [52] reported that  $\theta'$  phase ( $\text{Al}_2\text{Cu}$ ) completely dissolved into Al-1.7 at%Cu (at%, atom fraction) alloy matrix after 8 passes of equal channel angular pressing. Similarly, Wang's TEM work [42] showed that the pre-existing aging induced  $\eta'$  and  $\eta$  precipitates in AA 7055 (Al-7.76Zn-1.94Mg-2.35Cu) dissolved during surface abrasion and did not re-precipitate even after 42 months of natural aging. These work showed good agreement with our XRD results.

Peaks broadening caused by microstrain and grain refinement was observed. The values of  $\{\beta_{\text{hkl}}^2 - \beta_0^2\}$  as a function of Bragg angle,  $2\theta$ , are shown in Fig. 4c for AA2024. By fitting the data using Eq. (1), the average grain size and microstrain of peened AA2024 surface layer is determined as  $28.3 \pm 2.9 \text{ nm}$  and  $0.21 \pm 0.023\%$ , respectively, which are comparable with those values of AA7150 [25].

In addition, compared with the as-received, shifting of XRD peak position caused by USSP was observed for the alloys AA2024, AA7150 and pure Al, as clearly seen from Fig. 5. For AA2024 (Fig. 5a), there was no obvious shifting; For AA7150 (Fig. 5b), very obvious shifting was exhibited, all peaks shifted to the lower angle direction [25]. Peak position would shift when there are residual stress and the composition changes. It is well documented that compressive residual stress was introduced for SMAT/USSP treated alloys [4,53,54]. Compressive residual stress leads to decrease in interplanar distance  $d$ , and according to Bragg's law (Eq. (4)) the Bragg angle  $\theta$  increased.

$$2d \sin \theta = n\lambda \quad (4)$$

where  $d$  is interplanar distance of a crystal,  $n$  is a positive integer,  $\lambda$  is the wavelength of incident wave,  $\theta$  is the Bragg angle.

The XRD patterns of pure Al shown in Fig. 5c confirmed the effect of compressive residual stress to suppress vacancy effect, because all peaks of pure Al shifted to the higher angle direction after USSP treatment. Besides compressive residual stress and induced vacancies, surface segregation also influences peak shifting. XRD patterns confirmed that the segregated atoms in surface layer are in the form of solid solution. Due to larger atom radius of Zn, Cu and Fe than Al, the increment of these elements in Al matrix would increase interplanar distance, resulting in the shift of peaks to lower angles. As a comprehensive result of compressive stress, induced vacancies and surface segregation, all the peaks of AA7150 after USSP shifted to the lower angle direction [25].

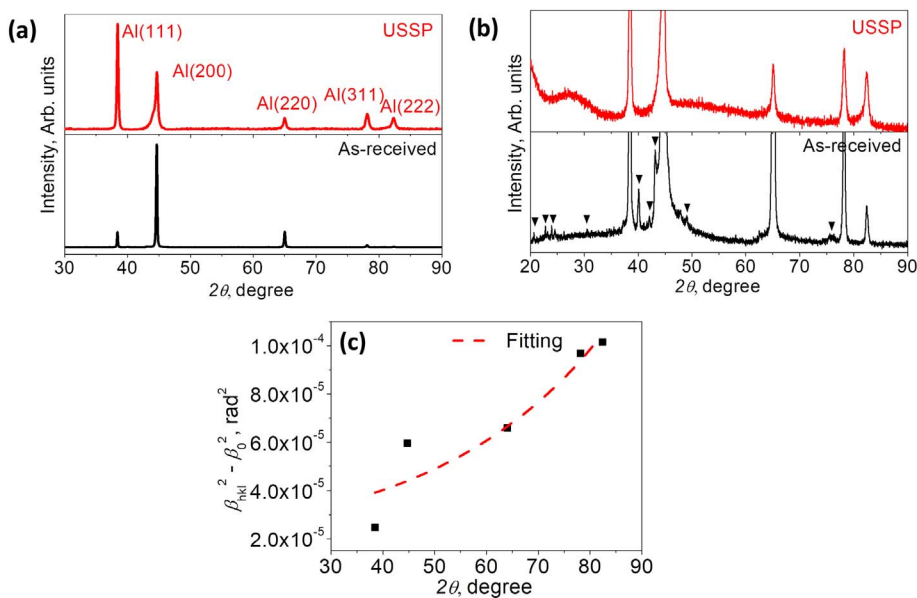


Fig. 4. (a) (b) XRD patterns of AA2024 after 1 month natural aging. (c) The values of  $\{\beta_{hkl}^2 - \beta_0^2\}$  as a function of Bragg angle  $2\theta$ .

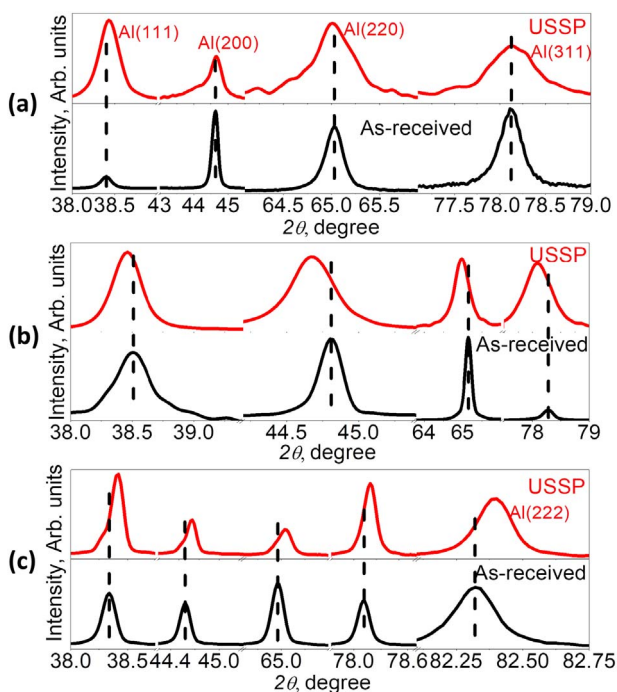


Fig. 5. XRD peaks shifting of Al alloys caused by USSP & natural aging: (a) AA2024; (b) AA7150 [25]; (c) pure Al.

Surface segregation phenomenon in AA2024 is less prominent than that in AA7150, thus the degree of peak shifting of AA2024 is between pure Al and AA7150.

### 3.5. Localized corrosion

After immersion in standard intergranular corrosion solution, the representative metallographically polished cross-section of as-received and peened AA2024 are respectively shown in Fig. 6a and Fig. 6b. The corrosion depth statistics is displayed in Fig. 6c. Severe intergranular corrosion occurred in the as-received AA2024 after immersion test. After USSP treatment, intergranular corrosion is significantly inhibited, the average corrosion depth reduced from  $192 \pm 54 \mu\text{m}$  to  $107 \pm 30 \mu\text{m}$ . The maximum corrosion depth reduced from  $283 \mu\text{m}$  to

$163 \mu\text{m}$ . Similar results can be found for AA7150 [22].

### 3.6. Open circuit potential

Galvanic corrosion may occur between peened layer and the substrate once localized corrosion initiates and propagates due to OCP change caused by USSP, as shown in Fig. 7. For AA2024 (Fig. 7a), OCP of peened layer is more positive than the untreated, thus the USSP layer will act as electron acceptor and accelerates the corrosion rate of substrate. Differently with AA2024, the USSP topmost layer of AA7150 will act as a sacrificial layer and protect the substrate beneath it during corrosion process, due to its more negative OCP as compared with substrate (Fig. 7b [25]). Note that the OCP fluctuation of as-received AA7150 might be due to the initiation and passivation of pits. The OCP trend revealed by Fig. 7 was confirmed by multiple parallel experiments. From the viewpoint of galvanic interaction, the peened layer of AA2024 is detrimental, while the peened layer of AA7150 is protective. We believe that, along with microstructure and composition, it is another reason for the fact that after immersion, localized corrosion of peened AA2024 can be observed to some extent, while for shot peened AA7150 it is eliminated [22].

OCP change caused by USSP of alloys is quite complex and influenced by multi-factors such as surface contamination, surface segregation of elements and the change of oxide film properties. OCP-composition relationships of AA2024 and AA7150 are shown in Fig. 8. OCP value of Fe or Ti is more anodic than that of Al, therefore the introduction of surface contamination are expected to shift OCP to the more anodic direction. As a result, influence of surface contamination on OCP is referred to as “Fe, Ti” in the first quadrant of OCP-composition coordinates. Several researchers [6,11,24,55,56] proposed the hypothesis that more compact and more passive oxide film formed after SMAT/SPD accounts for the OCP change. Assuming this proposal, it is reasonable to propose that OCP of Al alloys after USSP should shift to the more anodic direction. Thus, the effect of more passive oxide film is referred to as “ $\text{Al}_2\text{O}_3$ ” in first quadrant for both treated alloys. Cu and Fe segregated on the peened surface layer of AA2024. At any pH value, the enrichment of Cu and Fe would lead OCP value to shift to the more anodic direction. For AA2024, all the factors would result in the anodic shifting of OCP. As expected, after USSP, OCP of AA2024 shifts from  $-0.73$  to  $-0.66 \text{ V}_{\text{SCE}}$ . Differently with AA2024, due to the segregation of Zn on peened layer [25], OCP of AA7150 shifts to the more cathodic direction after USSP.

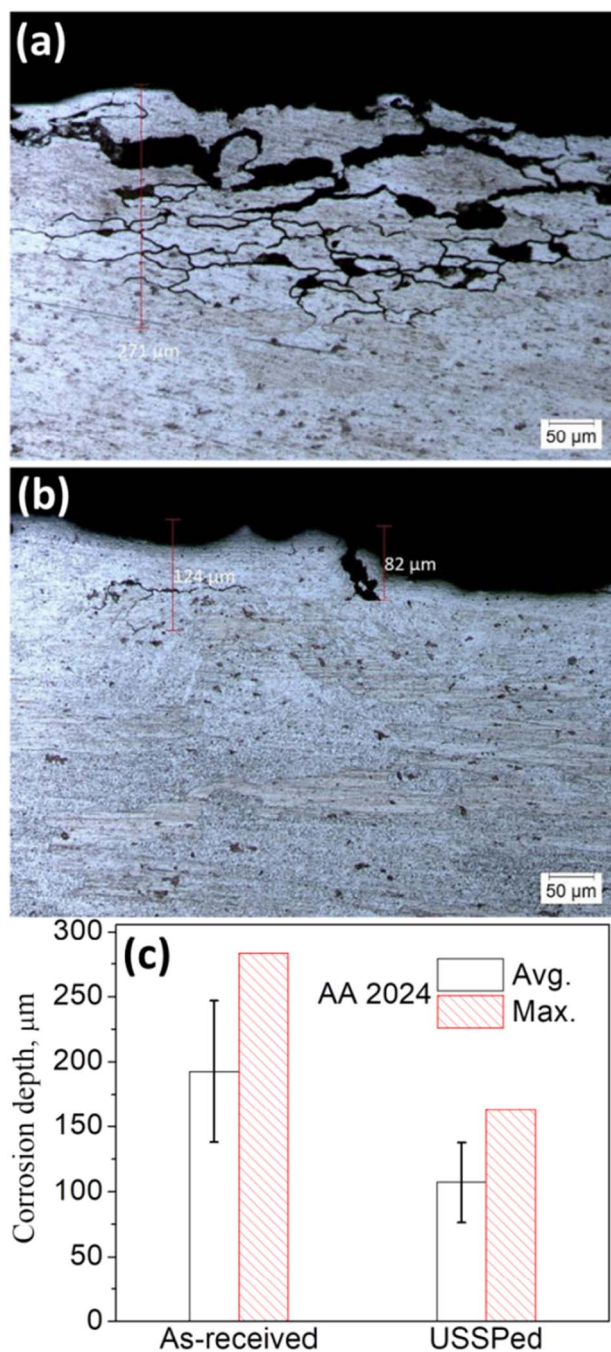


Fig. 6. The representative metallographically polished cross sections of AA2024 subjected to IGC test: (a) as-received; (b) USSP treated AA2024. (c) IGC depth statistics of AA2024 with and without USSP treatment.

### 3.7. EIS

In order to obtain accurate corrosion rate information, EIS characterization of AA2024 with and without USSP was performed in naturally aerated 3.5 wt% NaCl (pH = 5.8). The results are shown in Fig. 9. It can be clearly seen that corrosion rate of AA2024 increases by 2–3 times after USSP treatment, which is similar to the result of AA7150 [22]. Obviously, EIS result is contradictory with the improved localized resistance. This is because of the introduction of surface contamination during USSP treatment. The effect of surface contamination on corrosion rate of peened AA7150 alloy and its exfoliation process in solution containing  $H^+$  were systematically reported [22]. During immersion into standard IGC solution, the contamination layer exfoliates rapidly.

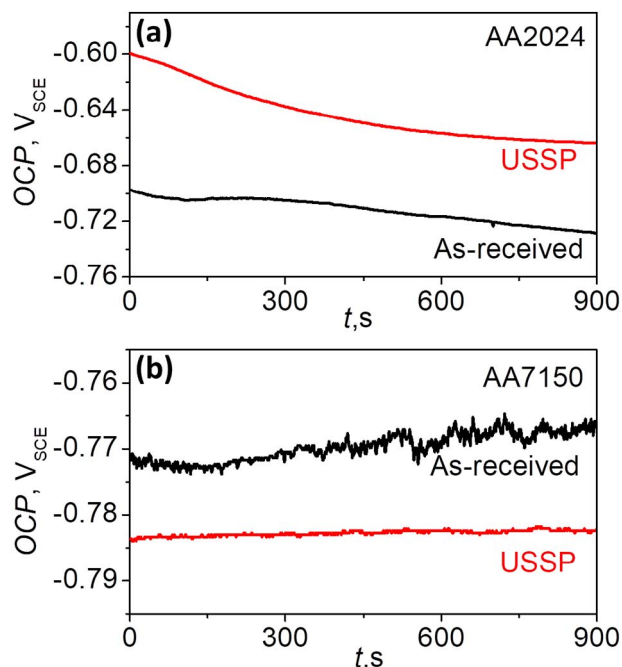


Fig. 7. Open circuit potential-time curves of alloys with and without USSP & 1 month natural aging treatments in naturally aerated 3.5 wt% NaCl solution (pH = 5.8) under room temperature: (a) AA2024; (b) AA7150 [25].

Therefore, it is believed that the effect of surface contamination layer on localized corrosion performance is insignificant. But, in practical service environment like marine atmosphere, the presence of Fe-rich surface contamination layer may result in a deleterious impact. This is due to the fact that under a moderate corrosion medium, the contamination layer can remain on the alloy surface for a long period. Fe-rich contamination layer will increase the corrosion rate of Al alloys due to galvanic interaction. So measures should be taken to avoid surface contamination for better performance against corrosion.

### 3.8. Polarization

Polarization curves of alloys shown in Fig. 10 reconfirmed the accelerated corrosion rate effect caused by surface contamination. Besides corrosion current density, another important parameter, pitting potential  $E_{pit}$ , can be derived from the polarization curves.  $E_{pit}$  is the lowest potential from which initiation of pitting is possible on a passive metal (CEN/TC262/WG1 N16 definition). This parameter characterizes the metal's resistance to pit initiation. Though not as obvious as the untreated sample due to the presence of surface contamination layer,  $E_{pit}$  of peened AA2024 still can be seen from Fig. 10a. The value of  $E_{pit}$  of peened AA2024 is  $\sim 50$  mV higher than that of the untreated counterpart. Similarly, the value of  $E_{pit}$  of AA7150 after USSP is  $\sim 70$  mV higher than its controlled sample, as indicated in Fig. 10b. The positive shifting of  $E_{pit}$  shows a good agreement with the improvement in localized corrosion of alloys. Our results are in accordance with Wang's work [57] which demonstrated that the 180 grit abraded overaged AA2024 with ASL (altered surface layer with 400 nm thick nanograins) showed a slightly higher  $E_{pit}$ , around 5–25 mV SCE, than the etched sample without ASL.

## 4. Discussion

SMAT/USSP is a technology that leads to grain refinement [27] and fragmentation of second phase particles [52], dissolves alloying elements into matrix [6,58,59], induces higher density of dislocations and grain boundaries [15,60], changes oxide film properties [61], induces

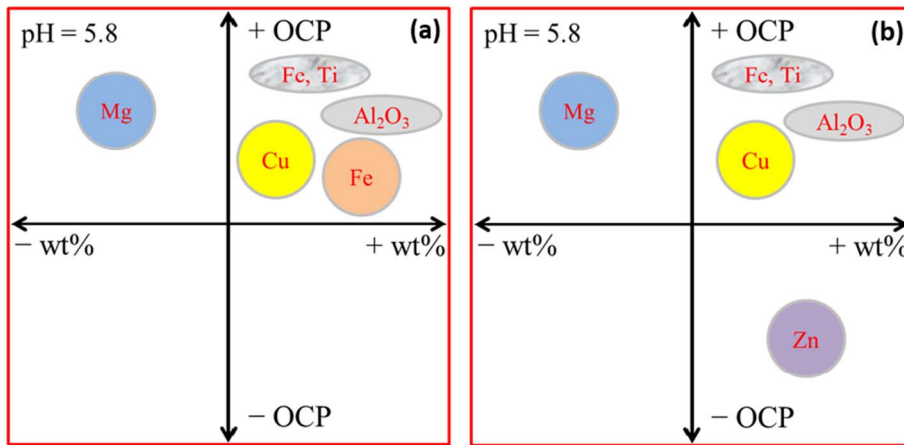


Fig. 8. OCP-composition relationship of USSP treated alloys when pH = 5.8: (a) AA2024; (b) AA7150 [25].

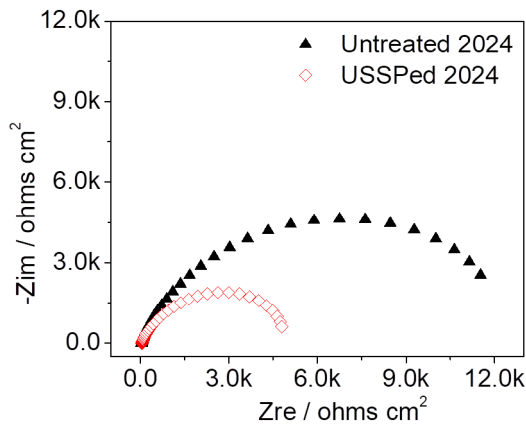


Fig. 9. EIS of AA2024 before and after USSP & 1 month natural aging treatments under naturally aerated 3.5 wt% NaCl solution (pH = 5.8).

compressive residual stress [4,35], increases surface roughness and defects density [60], introduces surface contamination [62–64] and leads to segregation [42,65] or dilution of segregation [24] on grain boundaries. All of these effects will influence corrosion performance of the alloys due to the fact that corrosion is a multifaceted and multidisciplinary subject which is affected by various factors.

Surface contamination mainly containing Fe-rich particles is a misleading factor for the corrosion assessment of USSP treated AA2024. As revealed by EIS and polarization results, the presence of Fe-rich particles on the very topmost surface layer increases AA2024 corrosion rate significantly. However, localized corrosion resistance of AA2024 actually is enhanced by USSP treatment according to the anodic shifting of pitting potential and IGC immersion results. Therefore, in surface severe plastic deformation area, only considering electrochemical

results probably would lead to an erroneous prediction of corrosion performance.

The nano/ultrafine grain layer beneath contamination layer is mainly accounted for the significant improvement in localized corrosion resistance. IGC is selective attack of the grain boundary zone, with no appreciable attack of the grain body or matrix [66]. The driving force is electrochemical and is the result of local cell action in the grain boundaries. For instance, in the 2024 alloy,  $\text{CuAl}_2$  precipitate is more noble than the matrix and acts as a cathode, accelerating the corrosion of a depleted zone adjacent to the grain boundary [66]. In AA7150, the compound  $\text{MgZn}_2$  is less noble than the matrix and acts as anodes and will be attacked [67]. After ultrasonic shot peening treatment, nanoprecipitates like  $\text{CuAl}_2$  and  $\text{MgZn}_2$  dissolved into Al matrix [28,68,69], which homogenizes microstructure and reduces the susceptibility of IGC. In addition, alloying elements of surface segregation layer are also in the form of solid solution, which is indicated by XRD results. Compressive residual stress, which is induced by USSP, is beneficial for IGC of alloys [4,70]. Therefore, to best of our knowledge, we believe that the improved localized corrosion resistance of AA2024 is mainly due to grain refinement and distortion effects, the absence of rolled texture, extended solid solubility, homogenization of surface layer microstructure and compressive residual stress caused by USSP.

Due to surface segregation, OCP of alloys changed after USSP treatment. Galvanic interaction between sub-surface layer and surface plays an important role in localized corrosion behaviour. For AA7150, USSP layer acts as a sacrificial layer and protects the substrate beneath it during localized corrosion, due to the surface segregation of Zn and Cu elements. For AA2024, USSP layer acts as electron acceptor and accelerate the corrosion rate of substrate, due to the surface segregation of Cu and Fe elements. In other words, from the viewpoint of galvanic corrosion, surface segregation layer for AA7150 is beneficial, while for AA2024 it is deleterious. That's the difference between the two studied

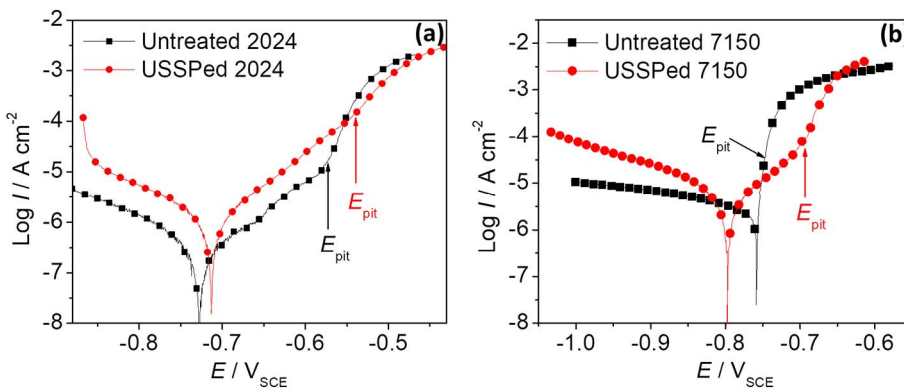


Fig. 10. Polarization curves of samples with and without USSP & 1 month natural aging treatments under naturally aerated 3.5 wt% NaCl solution (pH = 5.8): (a) AA2024; (b) AA7150.

alloys subjected to USSP treatment.

## 5. Conclusions

Surface nanocrystallization, surface segregation and surface contamination resulted on AA2024 through USSP treatment. Similar to AA7150, nearly random grain orientation was observed on peened AA2024 surface layer. Solid solubility of alloying elements in peened Al matrix extended significantly. Second phase particles,  $\theta$  and S phases of AA2024, dissolved into Al matrix after USSP. Due to surface contamination of iron-rich particles, corrosion rate of AA2024 increased by 2–3 times. For both treated alloys, pitting potential shifted to the more anodic direction. After USSP treatment, the average IGC depth of AA2024 reduced from  $192 \pm 54 \mu\text{m}$  to  $107 \pm 30 \mu\text{m}$ . The significant improvement in localized corrosion resistance is mainly attributed to grain refinement and dissolution of second phase particles caused by USSP.

Different surface segregation behaviours were observed for AA2024 and AA7150. After USSP and natural aging treatments, Cu and Fe segregated in AA2024 peened surface layer, while Zn and Cu segregated in AA7150 peened surface layer. As a result, OCP of peened AA2024 is more anodic than its untreated counterpart, while OCP of AA7150 shifts to more cathodic direction after USSP. OCP of alloy subjected to USSP treatment is influenced by multiple factors such as surface contamination, surface segregation and change of oxide film properties. Surface segregation, as driven by the decrease in Gibbs free energy of system, is a result of the accelerated diffusion of alloying elements from subsurface to surface layer along ‘short circuit’ paths like grain boundaries and dislocation pipes.

## Acknowledgment

This work was supported by the Center for Technology Development at Purdue University and the National Nature Science Foundation of China (No. 51474255). The financial support of the China Scholarship Council is also gratefully acknowledged. The authors would like to thank Mr. Zhenwei Wu at School of Chemical Engineering, Purdue University for the helpful discussions on XRD analysis. We also thank Dr. Shanshan Wang from Ohio State University for her constructive suggestions on paper structure. Prof. Wilson Xu is acknowledged for his suggestions and help on experiments. This paper is dedicated to my dear mentor, Prof. Qiyuan Chen, who unfortunately passed away in March, 2016. His guidance and wisdom will forever be memorized.

## References

- [1] N. Tao, Z. Wang, W. Tong, M. Sui, J. Lu, K. Lu, An investigation of surface nanocrystallization mechanism in Fe induced by surface mechanical attrition treatment, *Acta Mater.* 50 (2002) 4603–4616.
- [2] W. Tong, N. Tao, Z. Wang, J. Lu, K. Lu, Nitriding iron at lower temperatures, *Science* 299 (2003) 686–688.
- [3] B. Mordyuk, G. Prokopenko, Y.V. Milman, M. Iefimov, A. Sameljuk, Enhanced fatigue durability of Al-6Mg alloy by applying ultrasonic impact peening: effects of surface hardening and reinforcement with AlCuFe quasicrystalline particles, *Mater. Sci. Eng. A* 563 (2013) 138–146.
- [4] X. Liu, G. Frankel, Effects of compressive stress on localized corrosion in AA2024-T3, *Corros. Sci.* 48 (2006) 3309–3329.
- [5] Z. Ye, D. Liu, C. Li, X. Zhang, Z. Yang, M. Lei, Effect of shot peening and plasma electrolytic oxidation on the intergranular corrosion behavior of 7A85 aluminum alloy, *Acta Metall. Sin. (English Lett.)* 27 (2014) 705–713.
- [6] R. Gupta, D. Fabijanic, R. Zhang, N. Birbilis, Corrosion behaviour and hardness of in situ consolidated nanostructured Al and Al–Cr alloys produced via high-energy ball milling, *Corros. Sci.* 98 (2015) 643–650.
- [7] M. Abdulstaar, M. Mhaede, M. Wollmann, L. Wagner, Investigating the effects of bulk and surface severe plastic deformation on the fatigue, corrosion behaviour and corrosion fatigue of AA5083, *Surf. Coat. Technol.* 254 (2014) 244–251.
- [8] R. Waikar, Y. Guo, J. Liu, Z. Liu, Electrochemical corrosion behavior of surface nanocrystallized steel and aluminum alloys by air blast shot peening (ABSP), Flexible Automation (ISFA), International Symposium on, IEEE, 2016, pp. 359–365.
- [9] M. Navaser, M. Atapour, Effect of friction stir processing on pitting corrosion and intergranular attack of 7075 aluminum alloy, *Journal of Materials Science & Technology* 33 (2017) 155–165.
- [10] T. Balusamy, T.S. Narayanan, K. Ravichandran, I.S. Park, M.H. Lee, Influence of surface mechanical attrition treatment (SMAT) on the corrosion behaviour of AISI 304 stainless steel, *Corros. Sci.* 74 (2013) 332–344.
- [11] S. Kumar, K. Chattopadhyay, V. Singh, Effect of surface nanostructuring on corrosion behavior of Ti-6Al-4V alloy, *Mater. Charact.* 121 (2016) 23–30.
- [12] M. Ilieva, R. Radev, Effect of severe plastic deformation by ECAP on corrosion behaviour of aluminium alloy AA 7075, *Arch. Mater. Sci.* 56 (2016) 56.
- [13] N. Li, S. Shi, J. Luo, J. Lu, N. Wang, Effects of surface nanocrystallization on the corrosion behaviours of 316L and alloy 690, *Surf. Coat. Technol.* 309 (2017) 227–231.
- [14] T. Balusamy, S. Kumar, T.S. Narayanan, Effect of surface nanocrystallization on the corrosion behaviour of AISI 409 stainless steel, *Corros. Sci.* 52 (2010) 3826–3834.
- [15] Y. Estrin, A. Vinogradov, Extreme grain refinement by severe plastic deformation: a wealth of challenging science, *Acta Mater.* 61 (2013) 782–817.
- [16] S. Jelliti, C. Richard, D. Retraint, T. Roland, M. Chemkhi, C. Demangel, Effect of surface nanocrystallization on the corrosion behavior of Ti-6Al-4V titanium alloy, *Surf. Coat. Technol.* 224 (2013) 82–87.
- [17] C. Zhang, W. Song, F. Li, X. Zhao, Y. Wang, G. Xiao, Microstructure and corrosion properties of Ti-6Al-4V alloy by ultrasonic shot peening, *Int. J. Electrochem. Sci.* 10 (2015) 9167–9178.
- [18] A.A. Ahmed, M. Mhaede, M. Wollmann, L. Wagner, Effect of micro shot peening on the mechanical properties and corrosion behavior of two microstructure Ti-6Al-4V alloy, *Appl. Surf. Sci.* 363 (2016) 50–58.
- [19] P. Chui, K. Sun, C. Sun, X. Yang, T. Shan, Effect of surface nanocrystallization induced by fast multiple rotation rolling on hardness and corrosion behavior of 316L stainless steel, *Appl. Surf. Sci.* 257 (2011) 6787–6791.
- [20] D. Asquith, A. Yerokhin, J. Yates, A. Matthews, The effect of combined shot-peening and PEO treatment on the corrosion performance of 2024 Al alloy, *Thin Solid Films* 516 (2007) 417–421.
- [21] L. Wen, Y. Wang, Y. Zhou, L. Guo, J. Ouyang, Iron-rich layer introduced by SMAT and its effect on corrosion resistance and wear behavior of 2024 Al alloy, *Mater. Chem. Phys.* 126 (2011) 301–309.
- [22] Q. Sun, Q. Han, X. Liu, W. Xu, J. Li, The effect of surface contamination on corrosion performance of ultrasonic shot peened 7150 Al alloy, *Surf. Coat. Technol.* 328 (2017) 469–479.
- [23] K. Lu, J. Lu, Nanostructured surface layer on metallic materials induced by surface mechanical attrition treatment, *Mater. Sci. Eng. A* 375 (2004) 38–45.
- [24] R. Huang, Y. Han, The effect of SMAT-induced grain refinement and dislocations on the corrosion behavior of Ti-25Nb-3Mo-3Zr-2Sn alloy, *Mater. Sci. Eng. C* 33 (2013) 2353–2359.
- [25] Q. Sun, Q. Han, R. Xu, K. Zhao, J. Li, Localized corrosion behaviour of AA7150 after ultrasonic shot peening: corrosion depth vs. impact energy, *Corros. Sci.* 130 (2018) 218–230.
- [26] B.E. Warren, X-ray Diffraction, Courier Corporation, 1969.
- [27] X. Wu, N. Tao, Y. Hong, B. Xu, J. Lou, K. Lu, Microstructure and evolution of mechanically-induced ultrafine grain in surface layer of Al-alloy subjected to USSP, *Acta Mater.* 50 (2002) 2075–2084.
- [28] S.-S. Wang, J.-T. Jiang, G.-H. Fan, A. Panindre, G. Frankel, L. Zhen, Accelerated precipitation and growth of phases in an Al-Zn-Mg-Cu alloy processed by surface abrasion, *Acta Mater.* 131 (2017) 233–245.
- [29] M. Malaki, H. Ding, A review of ultrasonic peening treatment, *Mater. Des.* 87 (2015) 1072–1086.
- [30] R. Gupta, N. Birbilis, The influence of nanocrystalline structure and processing route on corrosion of stainless steel: a review, *Corros. Sci.* 92 (2015) 1–15.
- [31] M. Rakita, M. Wang, Q. Han, Y. Liu, F. Yin, Ultrasonic shot peening, *Int. J. Comput. Mater. Sci. Surf. Eng.* 5 (2013) 189–209.
- [32] L. Wen, Y. Wang, Y. Jin, X. Ren, Comparison of corrosion behaviour of nanocrystalline 2024-T4 Al alloy processed by surface mechanical attrition treatment with two different mediums, *Corros. Eng. Sci. Technol.* 50 (2015) 425–432.
- [33] W. Lei, Y. Yong, W. Yaming, J. Ying, Effect of nanocrystalline surface and iron-containing layer obtained by SMAT on tribological properties of 2024 Al alloy, *Rare Metal Mater. Eng.* 44 (2015) 1320–1325.
- [34] X. An, C. Rodopoulos, E. Statnikov, V. Vitazev, O. Korolkov, Study of the surface nanocrystallization induced by the eonix ultrasonic impact treatment on the near-surface of 2024-T351 aluminum alloy, *J. Mater. Eng. Perform.* 15 (2006) 355–364.
- [35] D. Fabijanic, A. Taylor, K. Ralston, M.-X. Zhang, N. Birbilis, Influence of surface mechanical attrition treatment attrition media on the surface contamination and corrosion of magnesium, *Corrosion* 69 (2012) 527–535.
- [36] O. Senkov, F. Froes, V. Stolyarov, R. Valiev, J. Liu, Microstructure and micro-hardness of an Al Fe alloy subjected to severe plastic deformation and aging, *Nanostruct. Mater.* 10 (1998) 691–698.
- [37] C. Zener, Theory of growth of spherical precipitates from solid solution, *J. Appl. Phys.* 20 (1949) 950–953.
- [38] D. Beke, I. Gödény, G. Erdelyi, F. Kedves, The temperature dependence of grain-boundary diffusion of 65Zn in polycrystalline aluminium, *Philos. Mag. A* 56 (1987) 659–671.
- [39] G. Stehchauner, E. Kozeschnik, Self-diffusion in grain boundaries and dislocation pipes in Al, Fe, and Ni and application to AlN precipitation in steel, *J. Mater. Eng. Perform.* 23 (2014) 1576–1579.
- [40] T. Fujita, Z. Horita, T.G. Langdon, Characteristics of diffusion in Al-Mg alloys with ultrafine grain sizes, *Philos. Mag. A* 82 (2002) 2249–2262.
- [41] N. Dolgopopolov, A. Rodin, A. Simanov, I. Gontar, Cu diffusion along Al grain boundaries, *Mater. Lett.* 62 (2008) 4477–4479.
- [42] S.-S. Wang, J.-T. Jiang, G.-H. Fan, A. Panindre, G. Frankel, L. Zhen, Accelerated

- precipitation and growth of phases in an Al-Zn-Mg-Cu alloy processed by surface abrasion, *Acta Mater.* 131 (2017) 233–245.
- [43] B. Straumal, B. Baretzky, A. Mazilkin, F. Phillipp, O. Kogtenkova, M. Volkov, R. Valiev, Formation of nanograin structure and decomposition of supersaturated solid solution during high pressure torsion of Al-Zn and Al-Mg alloys, *Acta Mater.* 52 (2004) 4469–4478.
- [44] A. Mazilkin, B. Straumal, E. Rabkin, B. Baretzky, S. Enders, S. Protasova, O. Kogtenkova, R. Valiev, Softening of nanostructured Al-Zn and Al-Mg alloys after severe plastic deformation, *Acta Mater.* 54 (2006) 3933–3939.
- [45] H.E. Swanson, E. Tatge, R.K. Fuyat, *Standard X-ray Diffraction Powder Patterns*, (1953).
- [46] Z. Liu, P. Chong, A. Butt, P. Skeldon, G. Thompson, Corrosion mechanism of laser-melted AA 2014 and AA 2024 alloys, *Appl. Surf. Sci.* 247 (2005) 294–299.
- [47] A. Meetsma, J. De Boer, S. Van Smaalen, Refinement of the crystal structure of tetragonal Al<sub>2</sub>Cu, *J. Solid State Chem.* 83 (1989) 370–372.
- [48] A. Alhamidi, Z. Horita, Grain refinement and high strain rate superplasticity in aluminium 2024 alloy processed by high-pressure torsion, *Mater. Sci. Eng. A* 622 (2015) 139–145.
- [49] D. Wang, Z. Ma, Effect of pre-strain on microstructure and stress corrosion cracking of over-aged 7050 aluminum alloy, *J. Alloys Compd.* 469 (2009) 445–450.
- [50] Y. Lang, Y. Cai, H. Cui, J. Zhang, Effect of strain-induced precipitation on the low angle grain boundary in AA7050 aluminum alloy, *Mater. Des.* 32 (2011) 4241–4246.
- [51] T. Ohba, Y. Kitano, Y. Komura, The charge-density study of the laves phases, MgZn<sub>2</sub> and MgCu<sub>2</sub>, *Acta Crystallogr., Sect. C: Cryst. Struct. Commun.* 40 (1984) 1–5.
- [52] M. Murayama, Z. Horita, K. Hono, Microstructure of two-phase Al–1.7 at% Cu alloy deformed by equal-channel angular pressing, *Acta Mater.* 49 (2001) 21–29.
- [53] J. Yu, G. Gou, L. Zhang, W. Zhang, H. Chen, Y. Yang, Ultrasonic impact treatment to improve stress corrosion cracking resistance of welded joints of aluminum alloy, *J. Mater. Eng. Perform.* 25 (2016) 3046–3056.
- [54] J. Wang, Y. Zhang, J. Chen, J. Zhou, M. Ge, Y. Lu, X. Li, Effects of laser shock peening on stress corrosion behavior of 7075 aluminum alloy laser welded joints, *Mater. Sci. Eng. A* 647 (2015) 7–14.
- [55] U. Trdan, J. Grum, SEM/EDS characterization of laser shock peening effect on localized corrosion of Al alloy in a near natural chloride environment, *Corros. Sci.* 82 (2014) 328–338.
- [56] U. Trdan, J. Grum, Evaluation of corrosion resistance of AA6082-T651 aluminium alloy after laser shock peening by means of cyclic polarisation and EIS methods, *Corros. Sci.* 59 (2012) 324–333.
- [57] S.-S. Wang, F. Yang, G. Frankel, Effect of altered surface layer on localized corrosion of aluminum alloy 2024, *J. Electrochem. Soc.* 164 (2017) C317–C323.
- [58] S. Bai, Z. Liu, X. Zhou, Y. Gu, D. Yu, Strain-induced dissolution of Cu–Mg co-clusters and dynamic recrystallization near a fatigue crack tip of an underaged Al–Cu–Mg alloy during cyclic loading at ambient temperature, *Scripta Mater.* 64 (2011) 1133–1136.
- [59] L. Zhou, G. Liu, X. Ma, K. Lu, Strain-induced refinement in a steel with spheroidal cementite subjected to surface mechanical attrition treatment, *Acta Mater.* 56 (2008) 78–87.
- [60] G. Gibson, K. Perkins, S. Gray, A. Leggett, Influence of shot peening on high-temperature corrosion and corrosion-fatigue of nickel based superalloy 720Li, *Mater. High Temp.* 33 (2016) 225–233.
- [61] L. Jinlong, L. Tongxiang, W. Chen, G. Ting, The passive film characteristics of several plastic deformation 2099 Al-Li alloy, *J. Alloys Compd.* 662 (2016) 143–149.
- [62] M. Vasylyev, B. Mordiyuk, S. Sidorenko, S. Voloshko, A. Burmak, Corrosion of 2024 alloy after ultrasonic impact cladding with iron, *Surf. Eng.* (2017) 1–6, <http://dx.doi.org/10.1080/02670844.2017.1334377>.
- [63] V. Zadorozhnyy, S. Kaloshkin, E. Kaevitser, S. Romankov, Coating of metals with intermetallics by mechanical alloying, *J. Alloys Compd.* 509 (2011) S507–S509.
- [64] S. Romankov, W. Sha, S. Kaloshkin, K. Kaevitser, Fabrication of Ti-Al coatings by mechanical alloying method, *Surf. Coat. Technol.* 201 (2006) 3235–3245.
- [65] M. Vasylyev, B. Mordiyuk, S. Sidorenko, S. Voloshko, A. Burmak, Peculiarities of structure and phase formations in the surface layers of 2024 alloy at UIT in various environments, *Metallofiz. Noveishie Tekhnol.* 39 (2017) 49–68, <http://dx.doi.org/10.15407/mfint.39.01.0049>.
- [66] R.W. Revie, H.H. Uhlig, *Uhlig's Corrosion Handbook*, John Wiley & Sons, 2011.
- [67] H.P. Godard, *The Corrosion of Light Metals*, John Wiley & Sons Inc, 1967.
- [68] V. Pandey, J. Singh, K. Chattopadhyay, N.S. Srinivas, V. Singh, Influence of ultrasonic shot peening on corrosion behavior of 7075 aluminum alloy, *J. Alloys Compd.* 723 (2017) 826–840.
- [69] B. Liu, X. Zhang, X. Zhou, T. Hashimoto, J. Wang, The corrosion behaviour of machined AA7150-T651 aluminium alloy, *Corros. Sci.* 126 (2017) 265–271.
- [70] X. Liu, G. Frankel, B. Zoofan, S. Rokhlin, Effect of applied tensile stress on intergranular corrosion of AA2024-T3, *Corros. Sci.* 46 (2004) 405–425.